Water Resources Research

Key Points:
- Pore-scale investigations were performed by MRI without additional contrast agents
- Dominant water loss processes were differentiated
- Liquid clusters were analyzed within the 3-D data sets

Supporting Information:
- Supporting Information S1

Correspondence to:
H. Horn,
harald.horn@kit.edu

Quantification of Evaporation and Drainage Processes in Unsaturated Porous Media Using Magnetic Resonance Imaging

Florian Ranzinger[1] ID, **Andrea Hille-Reichel[1]**, **Erwin Zehe[2]**, **Gisela Guthausen[1,3]** ID, and **Harald Horn[1,4]** ID

[1]Engler-Bunte-Institut, Water Chemistry and Water Technology, Karlsruhe Institute of Technology, Karlsruhe, Germany, [2]Institute of Water Resources and River Basin Management, Karlsruhe Institute of Technology, Karlsruhe, Germany, [3]Institute for Mechanical Process Engineering and Mechanics, Karlsruhe Institute of Technology, Karlsruhe, Germany, [4]Water Chemistry and Water Technology, DVGW Research Laboratories, Karlsruhe, Germany

Abstract The water loss in packed beds was studied spatially and time-resolved via magnetic resonance imaging on the pore scale. The packed beds were measured under water-saturated and unsaturated conditions, while the magnetic resonance method allowed a quantitative differentiation between air, liquid, and solid phases exploring the native contrast of the named phases without additional contrast agents. Beside a qualitative image comparison, subsequent quantitative image processing allowed for a detailed spatially resolved determination of water distribution, the differentiation between water transport processes, and the quantification of liquid clusters in 3-D. Results are presented for two packed beds that show significant differences in their evaporation and drainage dynamics, which are mainly determined by the physical properties of the packed beds. The water loss of the packed bed of 2–4 mm quartz particles reached a level below interpretability after 18.2 hr; meanwhile, a successive decrease of the largest liquid cluster volume from 82.5 to 0.7 mm^3 was observed. The water content of the packed bed of 2 mm glass spheres was still observable after 70.9 hr. During the experiment, no significant changes in the structure of the liquid clusters were measured. The current work displays the applicability of magnetic resonance imaging for pore-scale investigations without the addition of contrast agents.

1. Introduction

Imaging methods have a long tradition in analyzing structure and topology of porous media (Bastardie et al., 2005; Rabot et al., 2018; Vogel & Roth, 2001). With neutron radiography, microcomputer tomography (μ-CT), and magnetic resonance imaging (MRI), only few imaging methods have the potential to characterize the water phase in 3-D porous media (Kaestner et al., 2008; Koptyug, 2012; Rabot et al., 2018; Schaap et al., 2008; Shokri et al., 2008; Shokri & Sahimi, 2012). Over the past decade, especially, the interest in μ-CT has increased (Georgiadis et al., 2013; Koestel & Larsbo, 2014). μ-CT offers a spatial resolution of less than 1 μm, but a differentiation between water and air in the presence of highly X-ray absorbing materials remains challenging because of the low-contrast differences (Mayo et al., 2012; Yang et al., 2016). Commonly, a contrast enhancement is created by adding salt to the liquid phase (Georgiadis et al., 2013; Koestel & Larsbo, 2014; Shokri et al., 2010). The necessary concentrations are far higher than the salt concentrations normally present in soil. Shokri et al. (2010) started with a concentration of 4% w/w, which accumulated up to 12% w/w during the experiment (Shokri et al., 2010; Shokri & Sahimi, 2012). In addition, the hygroscopicity of salt influences the drying process. Important fluid properties like viscosity and evaporation enthalpy are increasing during the evaporation process due to the salt accumulation (Clarke & Glew, 1985). Methods based on μ-CT phase-contrast imaging might have the potential to avoid salt addition in future investigations (Mayo et al., 2012; Yang et al., 2016). However, ^1H MRI omits the use of contrast agents, as a signal is directly obtained from the water phase. The spatial resolution of MRI goes down to some tens of μm. Several studies of drying processes via MRI examine the water content within beds of particle sizes in the range of the spatial resolution or below by taking the partial volume affect into account (Faure & Coussot, 2010; Haber-Pohlmeier et al., 2017; Keita et al., 2013; Merz et al., 2014). The methodology can even be applied to investigate drying processes in porous media at the nanoscale (Thiery et al., 2017). However, some limitations remain for the application of MRI: (I) A high iron content of porous media causes fluctuations and static

distortions in the magnetic field; (II) a porescale investigation is only applicable for relatively coarse porous media due to the spatial resolution.

The current study displays MRI as a valuable tool for analyzing water release processes on the porescale. Thus, a spatially resolved differentiation between water, gaseous, and solid fractions was necessary, which lead to the usage of relatively large particles. Results are presented for two packed beds that are dominantly affected by different water loss processes, that is, evaporation and drainage. Further, analysis of water clusters was performed to reveal the dynamics of the water phase during the water loss.

2. Materials and Methods

2.1. Basic Principle of NMR/MRI

MRI is an imaging method based on nuclear magnetic resonance (NMR). In situ MRI is nondestructive with a spatial resolution down to some tens of μm. The technique allows for the observation of several parameters, for example, the distribution of NMR active nuclei, relaxation times, diffusion, or convection. NMR-active nuclei have an intrinsic magnetic moment. Some nuclei mainly explored in chemical analytics are ^{1}H,^{13}C,^{15}N, or ^{31}P. ^{1}H is commonly used because of its ubiquitous appearance in organic and many inorganic systems and the high physical sensitivity. This sensitivity is given by natural constants in form of the gyromagnetic ratio, essentially containing Planck's constant, the elementary electron charge, and the mass of the isotope. If NMR-active nuclei are exposed to a magnetic field, energy levels split up according to the number of nuclear spin states. In case of ^{1}H-NMR two energy levels exist due to nuclear spin ½ the population of which can be calculated according to the Boltzmann equation. The spin state parallel to the outer magnetic field is energetically slightly preferred. A macroscopic magnetization vector results along the magnetic field for a spin ensemble (Figure 1). The application of radio frequency pulses at the Larmor frequency brings the populations of the energy levels out of thermodynamic equilibrium, this state is named excitation. As in every thermodynamic system, the magnetization aims to return into the thermodynamic equilibrium, a process named relaxation. Relaxation starts immediately after the excitation. Two main phenomena are known, the transverse and the longitudinal relaxation. Both are substance specific and therefore well suited to create image contrast in MRI. The localization within the sample, that is, the spatial resolution in MRI, is achieved by magnetic field gradient pulses during the pulse sequence. Detailed descriptions of MRI are provided in several textbooks (Blümich, 2000; Callaghan, 1991; Kimmich, 1997).

2.2. NMR/MRI Setup

The packed beds were investigated in a 200 MHz superwide bore magnet equipped with an Avance HDIII console (Bruker BioSpin GmbH, Rheinstetten). The probe was a MICWB 40 with a 25 mm birdcage. Gradients up to 1.5 T/m were available for imaging. Measurements were performed using the "rapid acquisition with relaxation enhancement" pulse sequence in 2-D and 3-D. The sequence parameters are provided in the supporting information (S2).

2.3. Porous Media

Two different types of particles were used for the packed beds varying in material, diameter, size distribution, shape, and surface roughness (Table 1). The material properties, especially the surface roughness, were supported by stereomicroscopic images (SMT4, ASKANIA, and Mikroskop Technik Rathenow). The particles were selected in order to contain less than 1% of iron. As the iron atoms are rather isolated within the material, they are acting superparamagnetic and further not causing distortions during image acquisition.

2.4. Experimental Procedure

The particles were filled into a glass column with an inner diameter of 14 mm and a height of 200 mm. During packing, the column was shaken manually to compact the packed bed. The bottom of the glass column was connected to a tube and a syringe in order to saturate or drain the packed beds. A mesh with a mesh size of approximately 1.5 mm was positioned on top of the column for stabilization of the packed bed, particularly to prevent particle motion during saturation and draining. The mesh did not affect gas exchange with the surrounding environment. The packed beds were saturated with tap water by filling the columns from the lower end and up to the measurement region 20 mm below the top of the glass column (Figure 1). Thus, the upper 20 mm of the column consisted of unwetted particles, which inhibit Stage 1 evaporation
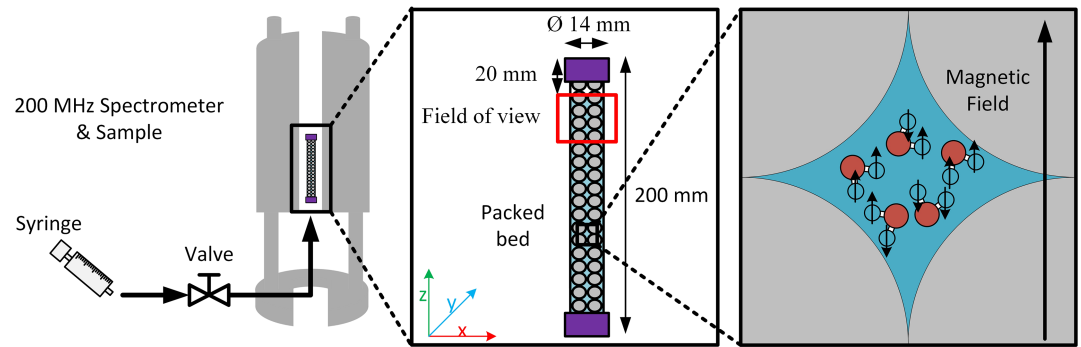
Figure 1. Illustration of the experimental setup (left), the saturated sample (middle), and the orientation of magnetic moments inside the sample (right) according to quantum mechanics. A signal is obtained from the water molecules. The spins of ^{1}H split up into two energy states within the magnetic field. The state parallel to the magnetic field is slightly preferred, leading to a macroscopic magnetization vector.

and impair the diffusional gas exchange during evaporation. Further, the 25 mm below the initial water level was observed by positioning the field of view. Reference images were taken under saturated condition. As no external heating was applied during the experiments, the water loss was initiated by manually draining the main water body with a syringe until a gas breakthrough through the whole column was observed. The removed water volume was typically around 12 ml. The retained water was around 0.7 ml for glass spheres and 1.7 ml for quartz particles. After the initial drainage, images were recorded to quantify the water loss within the field of view.

2.5. Estimation of Stage 2 Evaporation

The flux of water vapor caused by diffusion during Stage 2 evaporation was calculated according to equation (1) (Shokri, Lehmann, Vontobel, & Or, 2008):

$$J = \frac{\theta_a^{2.5}}{\varphi} D_{atm} \frac{C_{sat} - C_\infty}{z_{dried}}, \tag{1}$$

with θ_a the volumetric air content, φ the porosity, D_{atm} the vapor diffusion coefficient in free air at 25 °C, C_{sat} the saturated water vapor density at the secondary drying front, C_∞ the water vapor density above the packed bed, and z_{dried} the height of the dry surface layer zone. As already estimated in Shokri et al. (2008), volumetric air content and porosity were considered equal. Humidity above the packed bed was rather high (65%) due to a low restricted air exchange inside the spectrometer and no climate control inside the lab.

2.6. Data Analysis

Avizo 9.4 (FEI, Visualization Sciences Group) was used for image analysis. The first part of image analysis was the differentiation between the three different phases: air, water, and solid particles in the 2-D/3-D images. Images comprised 2^{15} intensity values. The first threshold was set in the reference images to differentiate between particles and water filled void space (Figure 2b): at 1,500 for the 2 mm glass spheres and at 1,300 for the 2–4 mm quartz particles. A second threshold was set in the images obtained during water loss, to distinguish between water and air inside the pore space: at 1,000 for the 2 mm glass spheres and at 800 for the 2–4 mm quartz particles. Its value for both segmentation steps is set slightly above the signal-to-noise level in order to make the measurements as sensitive to water as possible. Therefore, we take into account that the void space is overestimated in our analysis due to the partial volume effect and spatial resolution. The combination of both binary images allowed the distinction between particle, air, and water fractions (Figure 2c).

Table 1
Properties of the Particles and Packed Beds

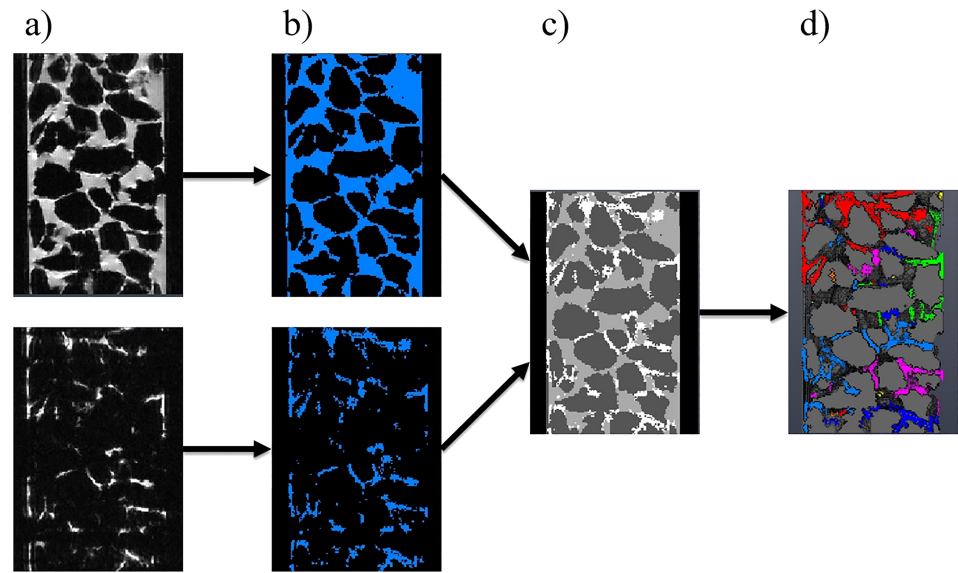|	2 mm glass spheres	2–4 mm quartz particles
Material	Glass	Quartz
Size distribution	2 ± 0.1 mm	2 – 4 mm
Shape	Spherical	Irregular
Surface roughness	Smooth	Rough
Estimated porosity of the packed bed by MRI	40.2%	44.6%
Weighed porosity of the packed bed	36.3%	41.2%
Maximum water content	9.2 ml	10.9 ml
Saturation after initial drainage	16.5%	19.4%

Figure 2. (a) Raw images are segmented into signal intense water and non-water-containing voxels in saturated conditions (upper image) and after initial drainage of the packed bed (lower image). The combination of the two binary images (b) allows to quantitatively differentiate between water (white), air (light gray), and particles (dark gray) (c). The water fraction is further processed to quantify liquid clusters (LCs) (d). Note that one color in (d) represents possibly more than one LC, as there were more LCs than colors available.

Adjustments were made because of slight particle displacements in the range of 1 to 2 voxels that occasionally occurred during initial drainage. The differentiation between pore space and particle fraction was adjusted once by segmentation of the first image of the drained packed bed in order to detect as much water as possible. Particle displacement at later times was not observed, as the columns were not mechanically stressed thereafter. As the water content decreases, so does the signal-to-noise ratio. At very low water content the signal-to-noise ratio was too low to allow for further quantification. These measurements were not considered in the quantitative analysis.

Besides the time resolved observation of the volume fractions, the liquid water saturation S was determined along the height z according to

$$S(z) = \frac{V_{\mathrm{H_2O}}(z)}{V_{\mathrm{Pore}}(z)} = \frac{V_{\mathrm{H_2O}}(z)}{V_{\mathrm{H_2O}}(z) + V_{\mathrm{Air}}(z)} \tag{2}$$

Here, all volume fractions at one height (z) were averaged. The saturation degree is given in percentage; the value 100 corresponds to the reference measurement at a certain height z and the value 0 to the case when no water is present.

The 3-D data sets were further quantified to obtain liquid clusters (LCs) and observe their behavior during water loss: A connected-component algorithm within the Avizo software quantified voxels attributed to the liquid phase that are directly connected to each other. The voxels were checked if at least one of the surrounding 26 voxels is also attributed to the liquid phase (Figure 2d). The connected water containing voxels are counted and summed up in one volume V_{LC}.

Two different representations were chosen in order to quantify the fracturing of LCs: Q_3 and V_{Class}. Q_3 is a cumulative function representing the fraction of LCs smaller and equal to a certain volume compared to the volume of all clusters. The function is used to characterize particle size distributions and is adapted for our approach (Allen, 1981). Here, Q_3 is plotted as a function of volume instead of diameter because of the irregular shape of the LCs. Thus, the definition of effective length scales and form factors was avoided (Figure 2d).
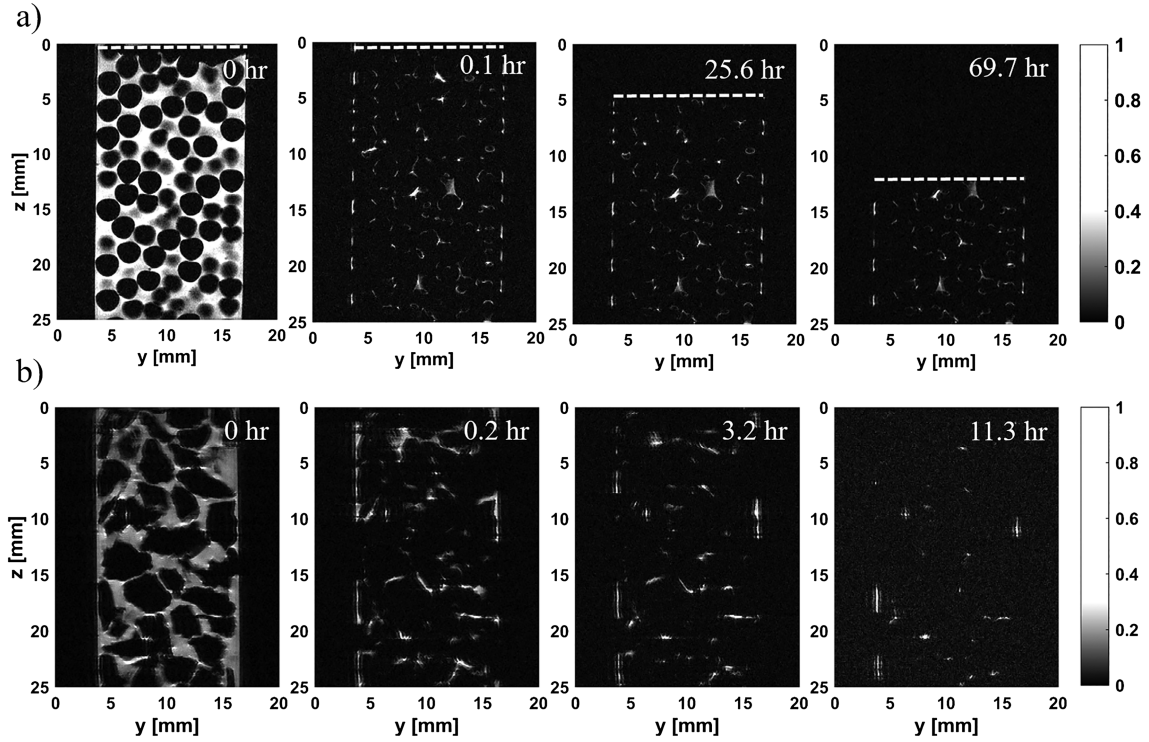
Figure 3. Cross-sectional planes through the packed beds in saturated condition (left images) and after the initial draining and subsequent water loss: (a) packed bed of 2 mm glass spheres after 0, 0.1, 25.6, and 69.7 hr; (b) packed bed of 2–4 mm quartz particles after 0, 0.2, 3.2, and 11.3 hr. The packed beds show different degrees of water retention and water loss. The packed bed of 2 mm glass spheres develops an evaporation front (dashed line), which shifts deeper into the column, while the water content in deeper regions stays constant. In contrast, the packed bed of 2–4 mm quartz particles loses water much faster and along the whole height.

$$Q_3(V_{LC}) = \frac{V_{LCi}}{V_{H_2O}}, \tag{3}$$

where V_{LCi} is the summation of all clusters smaller or equal to a certain cluster volume (V_{LC}) and V_{H_2O} is the total water volume (sum of all LC volumes) in the field of view. In the second representation, the LCs are classified into volume classes. All LCs within a class are summed up to one class volume V_{Class}.

$$V_{Class} = \sum_{V=V_i}^{V_{i+1}} V_{LC}(V) \tag{4}$$

Subdividing the LCs into classes and using absolute values supplements the cumulative distribution because the total loss of water can be displayed. The volumes were divided into four classes for every power of 10 in a range between 0.01 and 100 mm^3 resulting in 16 classes in total. The class limits of a given class were calculated by

$$\left.\begin{array}{l} V_i = 10^{\frac{i}{4} - 2} \\ V_{i+1} = 10^{\frac{i+1}{4} - 2} \end{array}\right\} \text{ with } i \in [0, 15] \tag{5}$$

3. Results and Discussion

3.1. Characterization of the Water Phase Within the Packed Bed

The MRI images (Figure 3) show the dynamics of the water phase. These images represent 2-D sections out of 3-D data sets. Under saturated conditions, the particles are clearly distinguishable from the bright pore space, which was completely filled with water.

The homogeneous particle size distribution in the packed bed of 2 mm glass spheres leads to rather enclosed pores where diffusion and advection are strongly hindered (Loskutov & Sevriugin, 2013). The remaining water is located mainly near the contact points of the glass spheres, 0.2 hr after the initial draining. Only
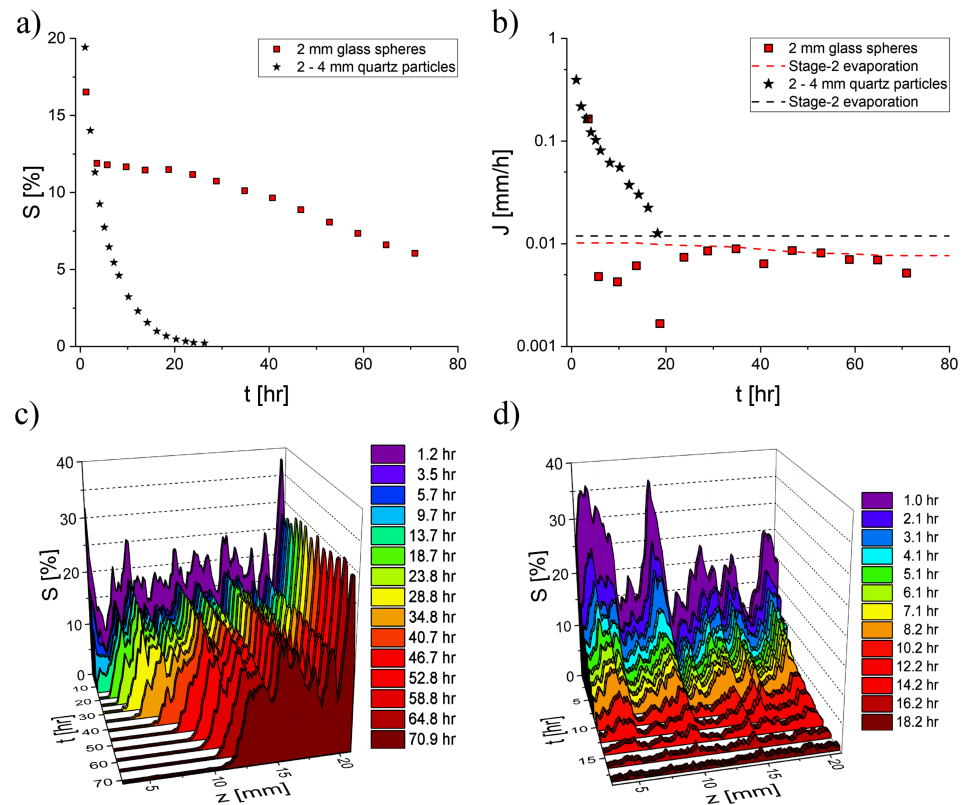
Figure 4. Quantification of 3-D MRI data. (a) Saturation within the field of view; (b) measured and estimated water loss (dashed lines) under the assumption of Stage 2 evaporation. Saturation development along the height z in the field of view for the packed bed of 2 mm glass spheres (c) and 2–4 mm quartz particles (d).

a few larger accumulations of water are observed. The evaporation front is marked with a white dashed line (Figure 3a), which is equal to the water level under saturated condition. As evaporation proceeds, the evaporation front propagates deeper inside the packed bed, while the water content in deeper regions stays constant. Image analysis reveals that the water content decreases continuously with time (Figure 4a). The water loss per time is in accordance with the estimated diffusion-driven Stage 2 evaporation (Figure 4b). Hence, evaporation is the dominant process in terms of water loss. It should be noticed that the analyzed area does not cover the whole evaporation front until 18.7 hr (Figure 4c). Thus, the water loss determined in the first 18.7 hr is lower compared to later measurements. Further, Figure 3c shows that the evaporation front is clearly visible as a sharp gradient affecting 1–2 mm along z and progressing deeper into the packed bed, while the saturation in deeper regions is not affected. Overall, the obtained data show the high accuracy of the MRI measurements.

The packed bed of irregularly shaped 2–4 mm quartz particles shows significantly different spatial characteristics and behavior regarding water retention and water loss (Figure 3b). The geometry of the particles induces a wide pore size distribution. In addition, the wall effect is recognizable; that is, the pore size distribution is much broader, comprising large pores as well as small pores close to the wall. After 0.2 hr, areas with large pores are completely invaded by air. Water is found in larger accumulations extended over more than one pore. As the process progresses, the water content decreases without developing a clear evaporation front. The loss of water also affects the signal-to-noise ratio in the MRI images, which is evident after 11.4 hr. Image analysis reveals a nonlinear decline in the water content (Figure 4a), which reaches a level below interpretability after 18.2 hr. The water loss per time is far faster than the estimated Stage 2 evaporation and rather shows any correlation with the water content. Therefore, percolation into deeper regions is the dominant effect. The height profile shows that accumulations of water inside the packed bed of the 2–4 mm quartz particles are noticeable, leading to characteristic minima and maxima (Figure 4d) caused
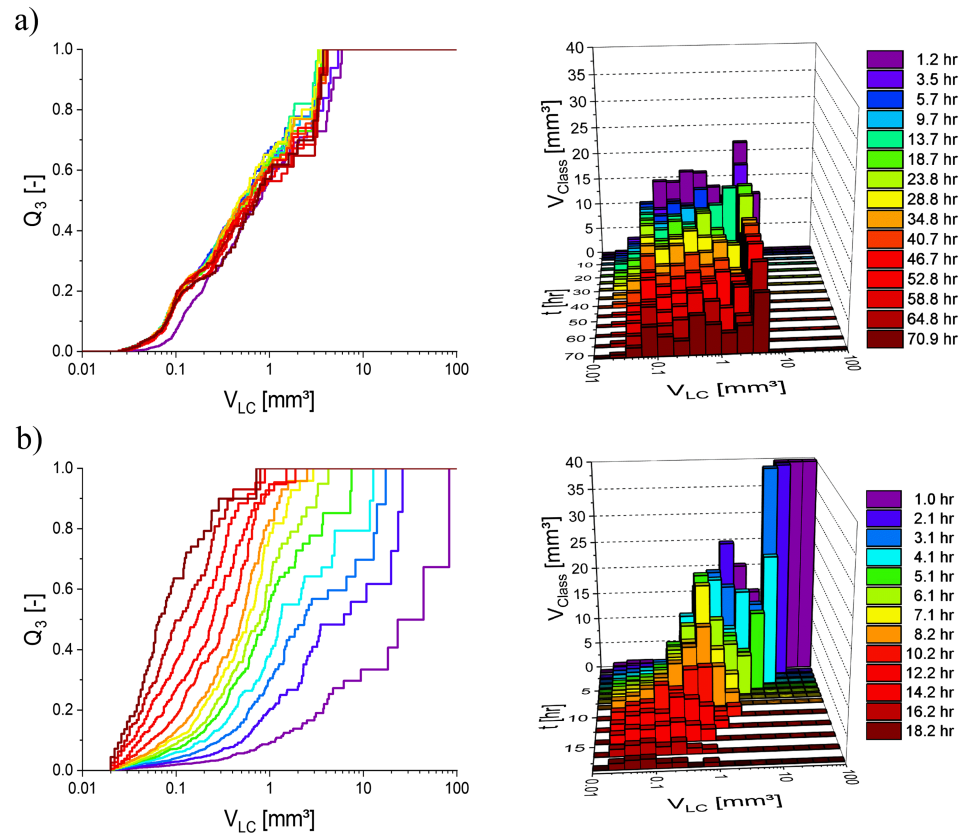
Figure 5. Cumulative volume distribution (left) and distribution of volume classes (right) of liquid clusters (LCs) during water loss in packed beds of (a) 2 mm glass spheres and (b) 2–4 mm quartz particles. Different behaviors of water loss are evident: Within the packed bed of 2 mm glass spheres, the LCs lose water equally distributed over all volume classes while the shape of the distributions remain fairly unchanged. Within the packed bed of 2–4 mm quartz particles, the LCs are fracturing and consequently experience a successive loss in volume.

by the bed structure. During water loss, lower saturation profiles are obtained along the whole height, while the local characteristics are maintained.

3.2. Evaporation- and Percolation-Driven Water Loss of LCs

As described in section 2.2, connected water voxels were counted and added to one volume, which was attributed to a LC. The packed beds show significant differences in fracturing because of packing structures and particle properties.

The LCs in the packed bed of 2 mm glass spheres do not exceed a size of 10 mm^3 (Figure 5a). As evaporation proceeds, no significant change inside the cumulative fraction is noticeable. The two first measurements show small differences likely due to percolation. As shown in Figures 4a and 4c, the measurement after 1.2 hr reveals a significantly higher water content. The class distribution indicates that all classes of LCs are losing water equally and no shift in the distribution is observed. This is consistent with the sharp evaporation frontier that shifts deeper into the column. The LCs at this front are evaporating first while no water uptake from below is evident. Dullien et al. (1989) already observed a negligible water transport between LCs in packed beds of smooth, homogeneous glass beads while the fluid saturation within packed beds of etched spheres kept decreasing with increasing applied capillary pressure (Dullien et al., 1989).

At the beginning of the experiment with the packed bed of 2–4 mm quartz particles, water is accumulated in large LCs (Figure 5b). About 70% of the total water content accumulated in LCs larger than 10 mm^3 while around 30% accumulated in the largest LC. Large LCs exceed the scale of the class distribution, but they can be distinguished in the cumulative distribution because of their large volumes. Both distributions show that fracturing and water loss of LCs led to a process that is observable in a

successive decrease of the LC volumes. For example, the volume of the largest LC decreased from 82.5 to 0.7 mm^3 after 18.2 hr. As water content decreases, the LCs lose volume. Connected pores might be invaded by air. Consequently, more LCs appear, and smaller volume classes temporarily increase the number of LCs (see Supporting Information S3).

4. Conclusions

The present study highlights MRI as a suitable analytical tool for noninvasive and nondestructive pore-scale investigations. The applicability of the obtained data is shown in the form of qualitative image comparison, quantitative observation of the water content, and differentiation between water transport processes and quantification of LCs in 3-D. ^{1}H density and relaxation were used as native contrast. Relaxation phenomena correlate with the volumetric water content in the porous media. For the measurement parameters applied in this study, the low volumetric water content results in a significant shortening of longitudinal relaxation, which enhances the signal obtained from the remaining water. The spatial resolution in combination with the relatively large particles enables a satisfactory representation of water distribution and LCs. To address packed beds with smaller particle sizes, most MRI studies do not resolve on the pore scale; thus, the water content within beds of particle sizes in the range of the spatial resolution or below is observed by taking the partial volume effect and relaxation phenomena into account.

As the image processing is also applicable for μ-CT data, it would be of interest to measure samples with μ-CT and MRI to compare both methods. Although μ-CT is generally capable to address smaller scales, it should be considered that MRI can be applied to investigate dynamic soil-biological interactions with respect to water content, as the sample is not exposed to potentially harmful radiation. In addition, evaporation-/drying-dominated processes can be studied, as no contrast agents are necessary and, thus, an accumulation of contrast agents can be avoided. Certainly, limitations due to paramagnetic compounds in the sample, temporal and spatial resolution should be considered. Potentially, the resolution of MRI measurements could be improved by allowing for a longer duration of the measurements and designing smaller samples. In the latter case, the wall effect on the packed bed will become more dominant.

References

Allen, T. (1981). *Particle size measurement* (3rd ed., Vol. 356, pp. 366-372). New York, NY: Chapman and Hall and Methuen.

Bastardie, F., Capowiez, Y., & Cluzeau, D. (2005). 3D characterisation of earthworm burrow systems in natural soil cores collected from a 12-year-old pasture. *Applied Soil Ecology*, *30*(1), 34–46.

Blümich, B. (2000). *NMR imaging of materials*. Oxford; New York: Clarendon Press; Oxford University Press.

Callaghan, P. T. (1991). *Principles of nuclear magnetic resonance microscopy*. New York: Oxford University Press.

Clarke, E. C. W., & Glew, D. N. (1985). Evaluation of the thermodynamic functions for aqueous sodium chloride from equilibrium and calorimetric measurements below 154 C. *Journal of Physical and Chemical Reference Data*, *14*(2), 489–610.

Dullien, F. A., Zarcone, C., Macdonald, I. F., Collins, A., & Bochard, R. D. (1989). The effects of surface roughness on the capillary pressure curves and the heights of capillary rise in glass bead packs. *Journal of Colloid and Interface Science*, *127*(2), 362–372.

Faure, P., & Coussot, P. (2010). Drying of a model soil. *Physical Review E*, *82*(3), 036303.

Georgiadis, A., Berg, S., Makurat, A., Maitland, G., & Ott, H. (2013). Pore-scale micro-computed-tomography imaging: Nonwetting-phase cluster-size distribution during drainage and imbibition. *Physical Review E*, *88*(3), 033002.

Haber-Pohlmeier, S., Vanderborght, J., & Pohlmeier, A. (2017). Quantitative mapping of solute accumulation in a soil-root system by magnetic resonance imaging. *Water Resources Research*, *53*, 7469–7480. https://doi.org/10.1002/2017WR020832

Kaestner, A., Lehmann, E., & Stampanoni, M. (2008). Imaging and image processing in porous media research. *Advances in Water Resources*, *31*(9), 1174–1187.

Keita, E., Faure, P., Rodts, S., & Coussot, P. (2013). MRI evidence for a receding-front effect in drying porous media. *Physical Review E*, *87*(6), 062303.

Kimmich, R. (1997). *NMR—Tomography diffusometry relaxometry*. Berlin: Springer Verlag.

Koestel, J., & Larsbo, M. (2014). Imaging and quantification of preferential solute transport in soil macropores. *Water Resources Research*, *50*, 4357–4378. https://doi.org/10.1002/2014WR015351

Koptyug, I. V. (2012). MRI of mass transport in porous media: Drying and sorption processes. *Progress in Nuclear Magnetic Resonance Spectroscopy*, *65*, 1–65.

Loskutov, V., & Sevriugin, V. (2013). A novel approach to interpretation of the time-dependent self-diffusion coefficient as a probe of porous media geometry. *Journal of Magnetic Resonance*, *230*, 1–9. https://doi.org/10.1016/j.jmr.2013.01.004

Mayo, S. C., Stevenson, A. W., & Wilkins, S. W. (2012). In-line phase-contrast X-ray imaging and tomography for materials science. *Materials*, *5*(5), 937–965. https://doi.org/10.3390/ma5050937

Merz, S., Pohlmeier, A., Vanderborght, J., van Dusschoten, D., & Vereecken, H. (2014). Moisture profiles of the upper soil layer during evaporation monitored by NMR. *Water Resources Research*, *50*, 5184–5195. https://doi.org/10.1002/2013WR014809

Rabot, E., Wiesmeier, M., Schlüter, S., & Vogel, H.-J. (2018). Soil structure as an indicator of soil functions: A review. *Geoderma*, *314*, 122–137.

Schaap, J., Lehmann, P., Kaestner, A., Vontobel, P., Hassanein, R., Frei, G., et al. (2008). Measuring the effect of structural connectivity on the water dynamics in heterogeneous porous media using speedy neutron tomography. *Advances in Water Resources*, *31*(9), 1233–1241.

Shokri, N., Lehmann, P., & Or, D. (2008). Effects of hydrophobic layers on evaporation from porous media. *Geophysical Research Letters*, *35*, L19407. https://doi.org/10.1029/2008GL035230

Shokri, N., Lehmann, P., & Or, D. (2010). Liquid-phase continuity and solute concentration dynamics during evaporation from porous media: Pore-scale processes near vaporization surface. *Physical Review E*, *81*(4), 046308.

Shokri, N., Lehmann, P., Vontobel, P., & Or, D. (2008). Drying front and water content dynamics during evaporation from sand delineated by neutron radiography. *Water Resources Research*, *44*, W06418. https://doi.org/10.1029/2007WR006385

Shokri, N., & Sahimi, M. (2012). Structure of drying fronts in three-dimensional porous media. *Physical Review E*, *85*(6), 066312.

Thiery, J., Rodts, S., Weitz, D., & Coussot, P. (2017). Drying regimes in homogeneous porous media from macro-to nanoscale. *Physical Review Fluids*, *2*(7), 074201.

Vogel, H.-J., & Roth, K. (2001). Quantitative morphology and network representation of soil pore structure. *Advances in Water Resources*, *24*(3), 233–242.

Yang, F., Griffa, M., Bonnin, A., Mokso, R., Di Bella, C., Münch, B., et al. (2016). Visualization of water drying in porous materials by X-ray phase contrast imaging. *Journal of Microscopy*, *261*(1), 88–104.